Zhao D, Hu Z, Chen G, Chen H, Feng X.

Coupling analysis between vessel motion and internal nonlinear sloshing for FLNG applications.

***Journal of Fluids and Structures* 2018, 76, 431-453.**

Coupling analysis between vessel motion and internal nonlinear sloshing for FLNG applications

Dongya Zhao[a,c], Zhiqiang Hu[b]*, Gang Chen[a, d], Xiaobo Chen[e], Xingya Feng[e]

[a] State Key Laboratory of Ocean Engineering, Shanghai Jiao Tong University, 800 Dongchuan Road, Shanghai, China

[b] School of Engineering, Newcastle University, Newcastle upon Tyne, NE1 7RU, UK

[c] Collaborative Innovation Center for Advanced Ship and Deep-Sea Exploration, Shanghai Jiao Tong University, Shanghai, China

[d] Marine Design & Research Institute of China, Shanghai, China

[e] Deepwater Technology Research Centre, Bureau Veritas, Singapore

Abstract

The coupling interaction between vessel motions and internal tank sloshing is of vital importance for Floating Liquefied Natural Gas (FLNG) system design and operation due to the exposure to diverse sea states at any filling level. A numerical code based on potential flow is developed in this study to investigate the coupling interaction between 6 degrees of freedom (DOF) vessel motions and internal nonlinear sloshing. The impulsive response function (IRF) method is adopted in the resolution for the 6 DOF vessel motions, and internal liquid sloshing is numerically solved with the boundary element method (BEM). The coupling interaction between vessel motions and internal sloshing is calculated in the time domain through an iteration strategy. For the purpose of validating the code and enabling a perceptual understanding of these coupling effects, experimental tests of a vessel with two rectangular tanks are conducted. The proposed code is also validated by previous numerical and experimental results. In addition, the coupling interaction characteristics of internal liquid sloshing and vessel motions are studied, and the sensitivities of coupling effects to filling levels and wave directions are also analyzed. Decreased natural roll motion frequency and response amplitude are excited in the liquid loading condition more than in the solid loading condition; sway motion has a decreased response in the natural sloshing frequency and a response peak in the frequency region that is higher than the natural sloshing frequency; heave motion is not sensitive to sloshing loads. Phase shift analysis reveals that phase shifts between the wave and the sloshing loads change rapidly near the natural roll frequency and natural sloshing frequency. Furthermore, the natural sloshing frequency varies with changes in the filling level, and the coupling effects become obvious when the natural sloshing frequency is close to main response frequency region of the vessel. Moreover, coupling effects under head wave conditions have similar properties to those under beam sea conditions, but the sensitivity of pitch motion to sloshing is much lower than that of roll motion.

Keywords: coupling interaction; sloshing; FLNG; vessel motions; potential flow; model test

1. Introduction

As a promising facility in exploiting offshore natural gas fields in deep water, an FLNG system equipped with liquefaction plants and LNG storage tanks has attractive advantages in developing remote and scattered natural gas fields. However, sloshing in the LNG tanks will

significantly affect the motion of the FLNG vessel. FLNG vessel has large ranges of filling levels during the production process. Particularly in the offloading operation, the filling level can change greatly within a relatively short period. Thus, the demand for accurate and efficient tools to predict the coupling responses of liquid loading FLNG vessels has been increasing in the literature.

The coupling of vessel motions and internal sloshing has been analyzed in using various methods. Malenica et al. (2003) and Newman (2005) conducted coupling analysis in the frequency domain, where both vessel motions and liquid tank sloshing are linearized. Zhao et al. (2011) and Hu et al. (2016) both used numerical models to analyze internal sloshing loads on FLNG vessel in the frequency domain, and experimental results were presented for comparison (Hu et al., 2016). The linearized vessel motion model has been proven to be efficient, and calculation in the time domain can be performed based on frequency-domain results using the IRF method (Cummins, 1962; Ogilvie, 1964). Nevertheless, because the sloshing nonlinearity can affect the accuracy of the coupling responses prediction, more researches have been conducted in the time domain and nonlinear sloshing has been taken into consideration. Because the computational fluid dynamics (CFD) method can address the complicated internal sloshing problem, many studies have used a combined linear vessel motion model and CFD solver to simulate the coupling between vessel motions and liquid sloshing. Kim et al. (2007), Lee et al. (2007) and Nam et al. (2009) adopted the SOLA scheme (Kim et al., 2001) to simulate sloshing in liquid tanks for the analysis of a liquid loading vessel. Nam et al. (2009) compared the numerical simulation results with experimental results of a ship equipped with two liquid tanks. Li et al. (2012) and Jiang et al. (2016) used OpenFOAM to investigate sloshing and coupling with linear vessel motions in the time domain. Jiang et al. (2016) found that impact loads may be important for structural safety but have little effect on the global responses of a ship. Cercos et al. (2016) considered nonlinear vessel motions and sloshing using SHIXDOF (nonlinear ship motion simulation program with six degrees of freedom) and a CFD approach based on a fully nonlinear SPH solver.

Although CFD solvers perform well in liquid sloshing prediction, they tend to consume large computational resources and have poor efficiency in dealing with an FLNG system with varying filling conditions during the offloading operations. Comparatively, numerical analysis based on potential theory has advantages in computing time. Rognebakke and Faltinsen (2003) studied partially filled rectangular tanks in waves numerically and experimentally. Nonlinear sloshing in tanks was solved with a multimodal approach proposed by Faltinsen and Timokha (2001). Mitra et al. (2012) simulated nonlinear sloshing based on potential flow, and nonlinear vessel motion was simulated using a hybrid marine control system, and responses in complex sea conditions were analyzed. Huang et al. (2012) and Zhao et al. (2014) assumed sloshing in a liquid tank as perfect flow and investigated the coupling of liquid loading in a rectangular tank both numerically and experimentally. Artificial damping was introduced in their numerical simulation to account for viscous damping effects in sloshing. In terms of sloshing effects on vessel motion responses, potential flow can give good results with high efficiency.

Experimental tests can provide a more reliable and perceptual understanding of coupling responses in a liquid loading vessel. Experimental research conducted by Rognebakke and Faltinsen (2003), Huang et al. (2012) and Zhao et al. (2014) simplified the liquid tank into two dimensions. Coupling with vessel's roll motion was not considered (Rognebakke and Faltinsen, 2003; Zhao et al., 2014). Nam et al. (2009) carried out experimental tests of a vessel with two

tanks in 3D, and ship motions were restricted to heave, roll and pitch. Coupling among 6 DOFs was not considered, which might also be of high importance for the coupling interaction results.

The objective of the study is to develop an accurate and efficient numerical model to address the coupling interaction of internal liquid sloshing and 6-DOF vessel motion with high efficiency. An impulsive response function is used in predicting vessel motions in the time domain, and sloshing liquid is solved based on potential flow theory. For the safe operation of equipment on the topside, strict regulations on the motions of FLNG vessel are required, and sloshing in LNG tanks must not be violent (Zhao, 2013). Moreover, the main concern of coupling analysis is the effects of sloshing on the global motion responses of a vessel, which are slightly affected by the impact of sloshing loads (Jiang et al., 2016). Therefore, the potential flow theory is applicable in this study. Experimental tests are also conducted to validate the proposed numerical model. Based on numerical and experimental results, the coupling mechanism and sensitivities to filling levels and wave directions are studied. The sloshing effects on a vessel's motions are closely related to the phase shift between the sloshing and vessel's motions, and coupling properties differ for different motion modes. The filling level will change the sloshing natural frequency, and different coupling results can be induced.

2. Mathematical formulation

Considering the coupling between different vessel motion modes (i.e., sway and roll) and their interaction with sloshing, a barge vessel with two rectangular tanks is simulated in this study. To describe the vessel motions and internal liquid tank sloshing in a numerical simulation, one global coordinate system, one vessel-fixed and two tank-fixed coordinate systems are defined, as shown in Fig. 1. The global coordinate system $O-XYZ$ is earth-fixed with the Z-axis pointing upward. The vessel-fixed coordinate system $o-xyz$ is located at the center of gravity of the vessel with ox and oy pointing to the bow and portside of the vessel, respectively. Coordinate systems $O-XYZ$ and $o-xyz$ coincide with each other in the initial condition. The tank-fixed coordinate systems $o_1-x_1y_1z_1$ and $o_2-x_2y_2z_2$ are located at the still free surface center and are parallel with the vessel-fixed coordinate system.

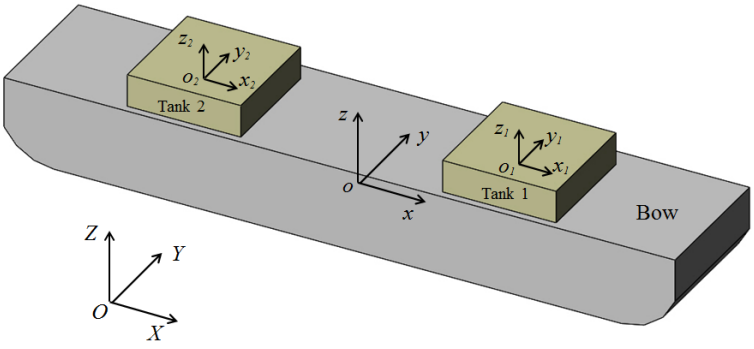

Fig. 1 Definition of coordinate system

2.1 Liquid sloshing

An internal sloshing problem in liquid tanks is solved based on potential theory by assuming the flow is inviscid and irrotational. In the calculation, a numerical model of a rectangular liquid tank with length B, width W and water depth D is built, as shown in Fig. 2.

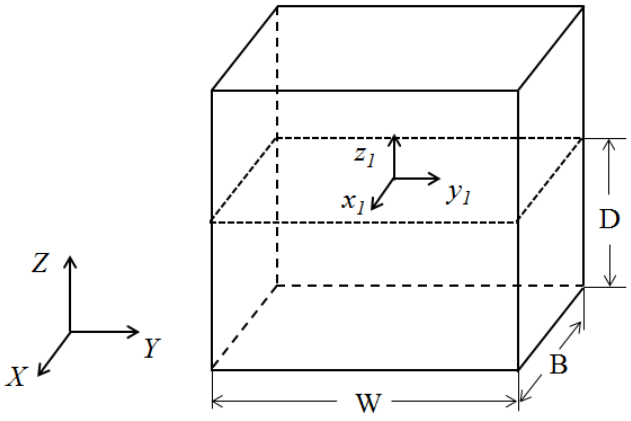

Fig. 2. Schematic of numerical tank model

For the convenience of coupling with vessel motion, the sloshing problem is solved in the tank-fixed coordinate. Velocity potential ϕ is decomposed as $\phi = \varphi + xu + yv + zw$. A boundary value problem of velocity potential in the tank-fixed coordinate system can be derived as follows:

In the fluid domain,

$$\nabla^2 \varphi = 0 \tag{1}$$

On the wall boundaries,

$$\frac{\partial \varphi}{\partial n} = (\boldsymbol{\omega} \times \mathbf{r}) \cdot \mathbf{n} \tag{2}$$

where $\mathbf{V} = [u, v, w]$ and $\boldsymbol{\omega} = [\omega_x, \omega_y, \omega_z]$ are translational and rotational velocities of the tank that correspond to the vessel's six motions, respectively. $\mathbf{n}$ is the unit normal vector pointing out of the tank walls, and $\mathbf{r}$ is the distance from the rotation center to the boundaries.

On the free surface S_F, dynamic and kinematic conditions are

$$\frac{\partial \varphi}{\partial t} - \boldsymbol{\omega} \times \mathbf{r} \cdot (\nabla \varphi + \mathbf{V}) + x\frac{du}{dt} + y\frac{dv}{dt} + \zeta\frac{dw}{dt} + \frac{1}{2}\nabla\varphi \cdot \nabla\varphi + \mathbf{k}_\theta \mathbf{g} \mathbf{r}_0 = 0 \tag{3}$$

$$\frac{\partial \zeta}{\partial t} + \frac{\partial \varphi}{\partial x}\cdot\frac{\partial \zeta}{\partial x} + \frac{\partial \varphi}{\partial y}\cdot\frac{\partial \zeta}{\partial y} - \frac{\partial \varphi}{\partial z} - \boldsymbol{\omega} \times \mathbf{r}_0 \cdot \nabla\zeta = 0 \tag{4}$$

$$\mathbf{k}_\theta = \begin{bmatrix} \cos\beta\cos\gamma & -\cos\beta\sin\gamma & \sin\beta \\ \sin\alpha\sin\beta\cos\gamma + \cos\alpha\sin\gamma & -\sin\alpha\sin\beta\sin\gamma + \cos\alpha\cos\gamma & -\sin\alpha\cos\beta \\ -\cos\alpha\sin\beta\cos\gamma + \sin\alpha\sin\gamma & \cos\alpha\sin\beta\sin\gamma + \sin\alpha\cos\gamma & \cos\alpha\cos\beta \end{bmatrix} \tag{5}$$

where $\mathbf{g}=[0 \quad 0 \quad g]$ and $\mathbf{r_0}=[0 \quad 0 \quad \zeta]$. ζ is the free surface elevation defined in the tank-fixed coordinate system.

Initial conditions of φ and wave elevation η on the free surface can be expressed as $\varphi=-xu-yv-zw$ and $\eta(x,y,0)=0$, respectively. After solving the velocity potential, hydrodynamic pressure on the wall boundaries can be obtained according to the Bernoulli equation:

$$-\frac{P}{\rho}=\frac{\partial\varphi}{\partial t}-\boldsymbol{\omega}\times\mathbf{r}\cdot\left(\nabla\varphi+\mathbf{V}\right)+x\frac{du}{dt}+y\frac{dv}{dt}+\zeta\frac{dw}{dt}+\frac{1}{2}\nabla\varphi\cdot\nabla\varphi+\mathbf{k_0}\mathbf{g}\mathbf{r}_0 \tag{6}$$

In this paper, the concept of acceleration potential is adopted in the calculation of $\partial\varphi/\partial t$, which could improve numerical stability and computational efficiency (Tanizawa, 1995). The acceleration potential is defined as follows:

$$\phi_a=\frac{\partial\phi}{\partial t}+\frac{1}{2}\nabla\phi\cdot\nabla\phi \tag{7}$$

As the nonlinear part of ϕ_a does not satisfy the Laplace equation in the fluid domain, the pseudo-acceleration potential $\varphi_a=\partial\varphi/\partial t$ is defined. Then, the solution of φ_a can be regarded as a similar boundary value problem as the solution of φ. In the tank-fixed coordinate system, the governing equations of φ_a can be obtained as follows:

In the fluid domain,

$$\nabla^2\varphi_a=0 \tag{8}$$

On the free surface,

$$\varphi_a=-x\frac{du}{dt}-y\frac{dv}{dt}-\zeta\frac{dw}{dt}-\frac{1}{2}\nabla\varphi\cdot\nabla\varphi-\mathbf{k_0}\mathbf{g}\mathbf{r}_0+\left(\boldsymbol{\omega}\times\mathbf{r}\right)\cdot\left(\nabla\varphi+\mathbf{V}\right) \tag{9}$$

On the wall boundaries,

$$\frac{\partial\varphi_a}{\partial n}=\mathbf{n}\cdot[\dot{\boldsymbol{\omega}}\times\mathbf{r}+2\boldsymbol{\omega}\times\mathbf{V}_r+\boldsymbol{\omega}\times\left(\boldsymbol{\omega}\times\mathbf{r}\right)-\left(\nabla\varphi\cdot\nabla\right)\nabla\varphi]+\mathbf{n}\cdot\nabla[\left(\boldsymbol{\omega}\times\mathbf{r}\right)\cdot\left(\nabla\varphi+\mathbf{V}\right)] \tag{10}$$

where $\mathbf{V}_r$ is the velocity of fluid observed in the tank-fixed coordinate system.

After obtaining hydrodynamic pressure, calculations can proceed to the next time step. The time derivative of potential on the free surface is obtained as follows:

$$\frac{d\varphi}{dt}=\frac{\partial\zeta}{\partial t}\frac{\partial\varphi}{\partial y}-x\frac{du}{dt}-y\frac{dv}{dt}-\zeta\frac{dw}{dt}-\frac{1}{2}\nabla\varphi\cdot\nabla\varphi-\mathbf{k_0}\mathbf{g}\mathbf{r}_0+\left(\boldsymbol{\omega}\times\mathbf{r}\right)\cdot\left(\nabla\varphi+\mathbf{V}\right) \tag{11}$$

For the convenience of mesh updating during calculation, free surface elevation is updated vertically in the tank-fixed coordinate:

$$\frac{d\zeta}{dt}=\frac{\partial\varphi}{\partial y}-\frac{\partial\zeta}{\partial x}\frac{\partial\varphi}{\partial x}-\frac{\partial\zeta}{\partial y}\frac{\partial\varphi}{\partial y}+\left(\boldsymbol{\omega}\times\mathbf{r}\right)\cdot\nabla\zeta \tag{12}$$

An artificial damping model is used to account for energy dissipation caused by fluid viscosity. A damping force that is proportional to particle velocity and has the opposite direction is

assumed on the free surface. With damping coefficient μ, Euler's equation can be expressed as follows:

$$\frac{Dw}{Dt} = -\frac{1}{\rho}\nabla p - g\nabla\zeta - \mu\nabla\varphi \tag{13}$$

2.2 Vessel motion

Vessel motion in waves is regarded as a linear system subject to wave excitation. In the time-domain calculation, an impulsive response function method based on frequency-domain results is used to deal with radiation forces. A frequency domain solution of vessel motion is required.

The linear incident wave potential can be written in a general form as follows:

$$\phi_0(x,y,z,t) = \frac{Ag}{\omega} e^{kz} \sin\left[k\left(x\cos\beta + y\sin\beta\right) - \omega t - \sigma\right] \tag{14}$$

where A, ω, k, β, and σ are the wave amplitude, frequency, wave number, head angle and phase shift, respectively.

The solutions for diffraction and radiation potential are typical boundary value problems. Wave-exciting forces, added mass μ_{ij} and radiation damping λ_{ij} in the frequency domain are computed using the panel program WADAM.

Using the IRF method, radiation forces in the time domain can be obtained. According to Newton's law, the motion equation can be expressed as follows:

$$\left[M_{ij} + \mu_{ij}(\infty)\right]\ddot{\xi}_j(t) + \int_0^t k_{ij}(t-\tau)\dot{\xi}_j(\tau)\,d_\tau + C_{ij}\xi_j(t) = F_j^{wave}(t) + F_j^{sloshing}(t), \quad i,j = 1,2,\cdots 6 \tag{15}$$

where M_{ij}, $\mu_{ij}(\infty)$, k_{ij} and C_{ij} are the total mass of the vessel including liquid mass, added mass at infinite frequency, retarded function, and hydrostatic restoring coefficients, respectively. $F_j^{sloshing}(t)$ accounts for sloshing effects on vessel motion and is calculated in the sloshing model described in Section 2.1.

Retarded function k_{ij} stands for the memory effects of past motions and can be calculated based on radiation damping coefficients:

$$k_{ij}(t) = \frac{2}{\pi}\int_0^\infty \lambda_{ij}(\omega)\cos(\omega t)\,d_\omega \tag{16}$$

where λ_{ij} is radiation damping in the frequency domain. Seventy frequencies are adopted in the integral with truncation frequency equal to 3.5 *rad/s*. Added mass in infinite frequency and retarded function has the following relationship:

$$\mu_{ij}(\infty) = \mu_{ij}(\omega) + \frac{1}{\omega}\int_0^\infty k_{ij}(t)\cos(\omega t)\,d_t \tag{17}$$

Viscous damping is not negligible for a vessel's roll motion in this study, and a commonly used equivalent linear damping coefficient is introduced as follows (Kim et al., 2007):

$$b_{44}^{v} = 2\gamma\sqrt{\left(M_{44} + \mu_{44}(\infty)\right)C_{44}} \tag{18}$$

where the γ is the ratio of viscous damping to critical damping coefficient. Viscous damping coefficients in surge and sway motion directions can be expressed as

$$b^{v} = \frac{1}{2}C_d \rho S \tag{19}$$

Where S stands for projected area normal to flow, and $C_d = 3$ is selected for the present vessel considering the vessel profile and assuming low Keulegan Carpenter number flow (Faltinsen, 1993). This type of viscous damping has less influence on steady responses but will contribute to dissipating transient motions, and steady solutions can be obtained. Soft numerical springs are used to restrict the surge, sway and yaw motions of the vessel so that monotonously increasing or decreasing motions can be prevented. The natural frequency of soft spring can be calculated as $\sqrt{C_{ii}^{spring} / \left(M_{ii} + \mu_{ii}(\infty)\right)}$, which is smaller than the first mode response frequencies of vessel motions and sloshing.

2.3 Coupling of vessel motion and sloshing

In the solution to (15), $F_j^{sloshing}(t)$ and vessel motions are coupled. An iteration strategy is adopted to account for the coupling between the vessel motions and sloshing.

In the iteration process, as shown in Fig. 3, vessel motions serve as the excitation on the liquid tank and sloshing loads are regarded as forces on the vessel in vessel motion calculations. The sloshing calculation is conducted in a tank-fixed coordinate system, and $F_j^{sloshing}(t)$ must be transferred to the coordinate system where vessel motions are solved. In addition, inertia forces of liquid have been considered in the first term on the left-hand side of (15) and need to be excluded from $F_j^{sloshing}(t)$ in the coupling calculation. The wave action part is obtained from the frequency results described in Section 2.2 and is not affected by the iteration calculation. The iteration calculation between vessel motions and sloshing loads is conducted in each step until convergence is obtained, which means the balance between forces and motions in (15) is achieved. After the iteration calculation, both vessel motions and internal sloshing are updated and the calculation proceeds to the next time step.

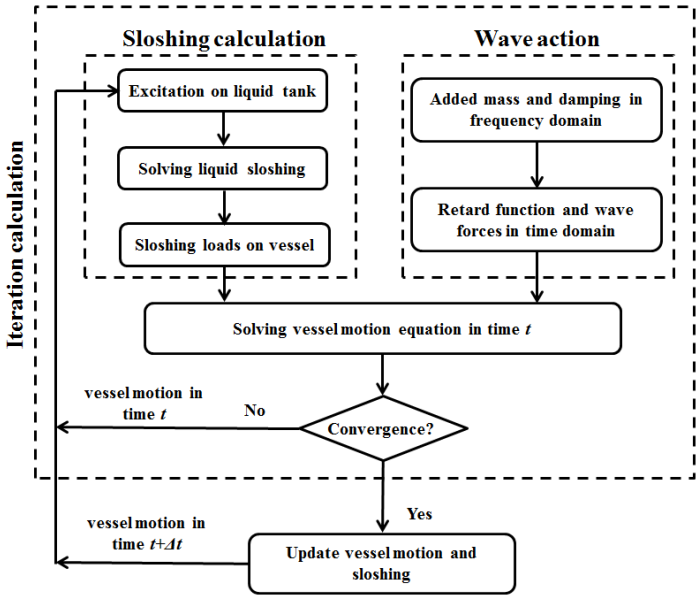

Fig. 3 Flow chart of coupled vessel motion and internal sloshing calculation

3. Numerical scheme for sloshing

The governing equations of both velocity potential and acceleration potential derived in Section 2.1 are boundary value problems, which are solved with the boundary element method in this study. By applying Green's second identity (Hunter and Pullan, 2001), the boundary integral equation can be derived:

$$c(p)\varphi(p) = \int_{\Gamma} \left(\frac{\partial \varphi(q)}{\partial n} G(p,q) - \varphi(q) \frac{\partial G(p,q)}{\partial n}\right) d\Gamma \tag{20}$$

where the solid angle $c(p)$ stands for the ratio of that angle occupied by the fluid to 4π; p and q are the source and field points in the respective boundaries. Γ denotes the boundaries of the fluid domain. $G(p,q)$ denotes Green's function, and the fundamental solution for the three dimensional Laplace equation can be written as follows:

$$G(p,q) = \frac{1}{4\pi r} \tag{21}$$

where $r = \sqrt{(x_p - x_q)^2 + (y_p - y_q)^2 + (z_p - z_q)^2}$ is the distance between point p and point q.

The direct method to obtain $c(p)$ is based on the unit normal vector on the elements around point p (Teng et al. 2006). In this study, the solid angle is solved using an indirect method. A non-zero constant potential is assumed over the boundaries Γ in (20), and no flux is produced over the boundaries. Then, the integral to solve $c(p)$ can be obtained by writing (20) as follows (Ning et al. 2010):

$$c(p) = -\int_{\Gamma} \frac{\partial G(p,q)}{\partial n} d\Gamma \tag{22}$$

The boundaries are then discretized into continuous and non-overlapping small elements. Triangular and rectangular elements are used in the discretization of free surfaces and wall boundaries, respectively, as shown in Fig. 4. This type of discretization is convenient for conducting mesh regeneration in the time-domain calculation and capturing a curved free-surface profile. Node points are distributed at the corners of each element. In this study, double and triple nodes are used in the boundaries and corners of the tank model, respectively (Grilli and Svendsen, 1990). Based on discretized elements, (20) can be rewritten as follows:

$$c(p_i)\varphi(p_i)+\sum_{j=1}^{N_e}\int_{\Gamma_j}\varphi(q)\frac{\partial G(p,q)}{\partial n}d\Gamma=\sum_{j=1}^{N_e}\int_{\Gamma_j}\frac{\partial\varphi(q)}{\partial n}G(p,q)d\Gamma \tag{23}$$

where N_e is the total number of elements on the wetted boundary.

Each element in (23) is mapped onto a two-dimensional plane (ξ,η), and the physical parameters in the element can be interpolated using a shape function as $\psi(\xi,\eta)=\sum_{k=1}^{K}N_k(\xi,\eta)\psi_k$, where ψ represents the physical parameters such as coordinates x, y, z and the velocity potential φ. The shape function $N_k(\xi,\eta)$ can be expressed in triangular and rectangular elements as follows:

$$\begin{cases}N_1(\xi,\eta)=1-\xi-\eta\\ N_2(\xi,\eta)=\xi\\ N_3(\xi,\eta)=\eta\end{cases}\text{ for triangular element;}\quad\begin{cases}N_1(\xi,\eta)=(1-\xi)(1-\eta)/4\\ N_2(\xi,\eta)=(1+\xi)(1-\eta)/4\\ N_3(\xi,\eta)=(1+\xi)(1+\eta)/4\\ N_4(\xi,\eta)=(1-\xi)(1+\eta)/4\end{cases}\text{ for rectangular element} \tag{24}$$

Then, (23) can be written in the following form:

$$c(p_i)\varphi(p_i)+\sum_{j=1}^{N_e}\sum_{k=1}^{K}a_{ij}^{k}\varphi_{jk}=\sum_{j=1}^{N_e}\sum_{k=1}^{K}b_{ij}^{k}\frac{\partial\varphi_{jk}}{\partial n} \tag{25}$$

where $a_{ij}^{k}=\iint_{\Gamma_j}N_k(\xi,\eta)\frac{\partial G}{\partial n}\left|J(\xi,\eta)\right|d_{\xi}d_{\eta}$ and $b_{ij}^{k}=\iint_{\Gamma_j}N_k(\xi,\eta)\mathrm{G}\left|J(\xi,\eta)\right|d_{\xi}d_{\eta}$ are integrals in each element that can be calculated using the Gaussian integral. Then, (25) can be written in the form of a system of equations as follows:

$$\sum_{j=1}^{N_p}G_{ij}\varphi_j=\sum_{j=1}^{N_p}H_{ij}\frac{\partial\varphi_j}{\partial n}\ \text{for } i=1,2,\ldots N_p \tag{26}$$

where $G_{ij}=c_i\delta_{ij}+\sum_{j=1}^{N_e}a_{ij}^{k}$ and $H_{ij}=\sum_{j=1}^{N_e}b_{ij}^{k}$ are coefficients of the linear equation system, and N_p is the total number of nodes.

The boundary conditions of $\varphi\big|_f$ and $\partial\varphi/\partial n\big|_w$ are given in (3) and (2), respectively, and (26) can be rearranged to solve $\partial\varphi/\partial n\big|_f$ and $\varphi\big|_w$ as follows:

$$\begin{bmatrix} -H_1 & G_2 \end{bmatrix} \begin{bmatrix} \partial\varphi/\partial n\big|_f \\ \varphi\big|_w \end{bmatrix} = \begin{bmatrix} -G_1 & H_2 \end{bmatrix} \begin{bmatrix} \varphi\big|_f \\ \partial\varphi/\partial n\big|_w \end{bmatrix} \tag{27}$$

$$G_1=G_{ij},\ H_1=H_{ij} \quad \text{for } i = 1,2,...,N_p;\ j = 1,2,...,N_{pf} \tag{28}$$

$$G_2=G_{ij},\ H_2=H_{ij} \quad \text{for } i = 1,2,...,N_p;\ j = N_{pf}+1, N_{pf}+2,...,N_p \tag{29}$$

Where N_{pf} is the node number on the free surface.

Acceleration potential φ_a can be solved similarly to the potential problem. $\varphi_a\big|_f$ and $\partial\varphi_a/\partial n\big|_w$ are given in (9) and (10), respectively. Since the acceleration potential and potential are solved in the same mesh scheme, the equation system of acceleration potential has the same coefficients in (27). Thus, not much more computational resources are needed.

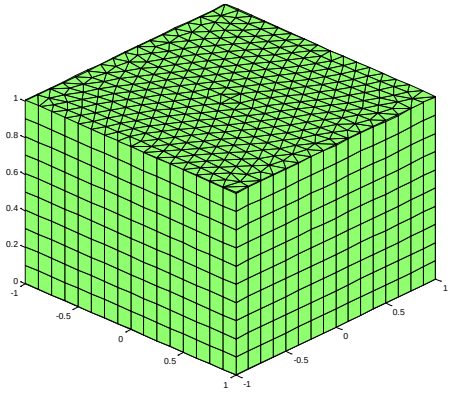

Fig. 4. Mesh model of 3D tank

4. Experimental setup

To validate the numerical code and obtain a better understanding of coupling effects in a liquid loading vessel, experimental tests are conducted in the Deepwater Offshore Basin at Shanghai Jiao Tong University. The basin is 50 m long, 40 m wide and 10 m in depth. Two adjacent basin banks are installed with wave maker panels and the other two banks are installed with wave absorbers to dissipate the wave reflections. The model scale of an FLNG vessel with two liquid tanks is selected as 1:60. Configurations of the vessel are presented in Fig. 5. Two rectangular tanks are installed symmetrically about the transverse section with a filling level of 66.7%. The main particulars of the vessel and tanks are listed in Table 1. Solid loading tests are also included in the experiment for comparison. Solid and liquid loading conditions have the same inertia particulars assuming the liquid in tanks is frozen.

White noise waves are generated in the experimental tests to obtain vessel motions and sloshing responses in a wide frequency range that can cover the main response frequencies of both vessel motion and sloshing responses. Beam, quarter and head sea conditions are considered in the experiment. A comparison of wave spectra is presented in Fig. 6, and the good agreement demonstrates the accuracy of waves generated. The ship is restricted by horizontal soft springs to prevent drift motions and ensure that first-order motions are not greatly influenced. Wave probes are installed in the liquid tank close to the bow (marked as ‘T’ in Fig. 5 (b)) to measure sloshing

wave elevation in representative positions, and sloshing responses in these two tanks will be much more similar for the symmetry of vessel profile and tank locations about midship.

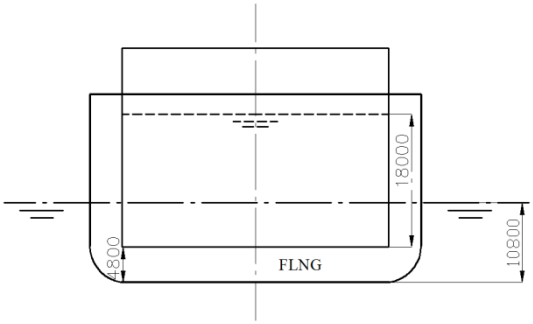

(a) Front view

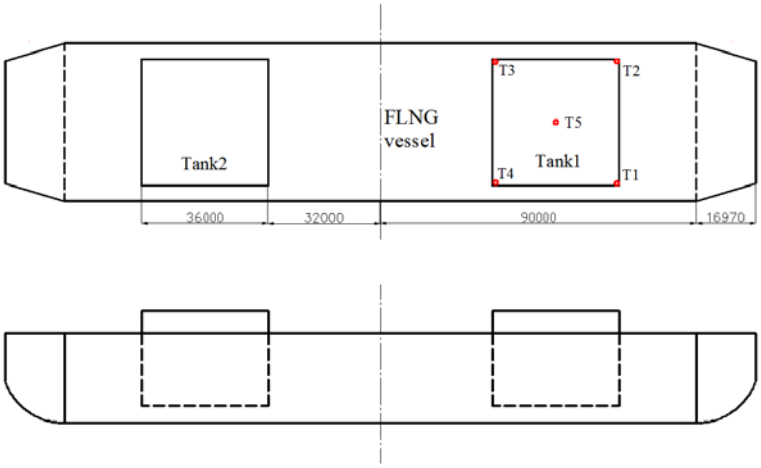

(b) Top view and side view

Fig. 5 Profiles of FLNG vessel with two rectangular tanks (unit: mm)

Table 1 Main particulars of FLNG vessel and LNG tank

Main particulars	Prototype	Model
Length (m)	213.94	3.566
Width (m)	44.8	0.747
Draft (m)	10.8	0.18
Displacement (t)	98923.1	0.447
Roll gravity radius (m)	16	0.267
Pitch gravity radius (m)	60	1
Yaw gravity radius (m)	60	1
Tank length (m)	36	0.6
Tank width (m)	36	0.6
Tank height (m)	27	0.45

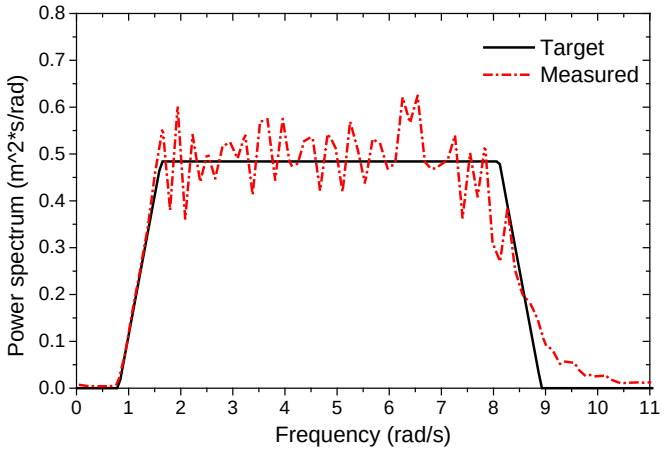

Fig. 6 Spectra of white noise wave in beam sea condition

5. Numerical validation

Validations of the proposed numerical model are conducted by comparing the numerical simulation results with the results from previous studies.

First, numerical predictions of sloshing under forced translational excitations are validated. For sloshing cases with different tanks size and excitation, convergence analyses are conducted to guarantee the mesh size and time step convergence. Sloshing responses in a three-dimensional liquid tank are compared with the calculation results of Wu et al. (1998) using the FEM method. Particulars of the tank are non-dimensionalized based on water depth D and gravity g as follows: $(B,W)\to(B,W)/D$, $t\to t/\sqrt{g/D}$. The convergence results of a tank with $B=W=2$ are presented in Fig. 7. The particulars of the sinusoidal excitation on the tank are $A_x=0.002$ and $\omega_x=\omega_{10}$ (5.316*rad/s*). Wave elevation histories in corner $(B/2,-D/2)$ and wave profile at the time $t=39.46$ show that the mesh number $14\times14\times8$ and time step $\Delta t=0.0443$ can give convergent results. In the validation tests, $B=W=4$ is selected and displacements of the tank in the x and y directions are in sinusoidal form as $d_x(t)=A_x\sin(\omega_x t)$ and $d_y(t)=A_y\sin(\omega_y t)$, respectively, with $A_x=0.0372$, $\omega_x=\omega_{10}$, $A_y=0.0182$, $\omega_y=\omega_{01}$. Element numbers along the tank's width, length and water depth are set as $14\times14\times8$, and the time step is set as $\Delta t=0.0443$. Wave elevation histories in two corners are presented in Fig. 8, and good agreements are obtained.

Second, free surface elevation in sloshing under forced rotational excitations is validated. A two-dimensional tank subjected to rotational excitation studied by Nakayama and Washizu (1981) is chosen. The tank has parameters $B=0.9m$, $D=0.6m$. The rotational excitation on the tank is applied in cosine form as $A_{\theta x}(t)=\theta_x\cos(\omega_{\theta x}t)$, where $\theta_x=0.8deg$ and $\omega_{\theta x}=5.5rad/s$. In the proposed numerical model, a numerical tank with $B\times W\times D=0.9m\times0.3m\times0.6m$ is built and the mesh is set as $18\times6\times12$. Wave elevation histories at the corner $(B/2,-D/2)$ are presented in Fig. 9, and good agreement is obtained. Moreover, sloshing loads on the tank wall under forced rotational excitation are validated. Experimental and numerical studies conducted by Chen et al.

(2007) are chosen. The dimensions of the liquid tank are $B \times W \times D = 1m \times 1m \times 0.3m$ and the mesh is set as $15 \times 15 \times 5$ in the present simulation. Rotational excitation on the tank is in sinusoidal form as $A_{\theta x}(t) = \theta_x \sin(\omega_{\theta x} t)$ with $\theta_x = 5deg$. Two cases with $\omega_{\theta x} = 0.95 rad/s$ and $\omega_{\theta x} = 3.09 rad/s$ are selected. Time series of the pressure load on the left wall of $0.1m$ forming the initial free surface are captured. Fig. 10 shows that present numerical results with $\omega_{\theta x} = 0.95 rad/s$ agree well with experimental and numerical results in Chen et al. (2013). When excitation increases to $\omega_{\theta x} = 3.09 rad/s$, larger sloshing is induced, and pressure fluctuation appears. The general tendency and amplitude of sloshing pressure are well simulated, which proves the validity of the proposed numerical model.

It should be noted that the applicability of the proposed numerical model is limited to sloshing with single-valued free surface profile. Violent sloshing that includes wave break and overturning is not considered in the present study. Thus, extremely shallow loading conditions where the tank bottom may be out of water are also beyond the capability of the present model.

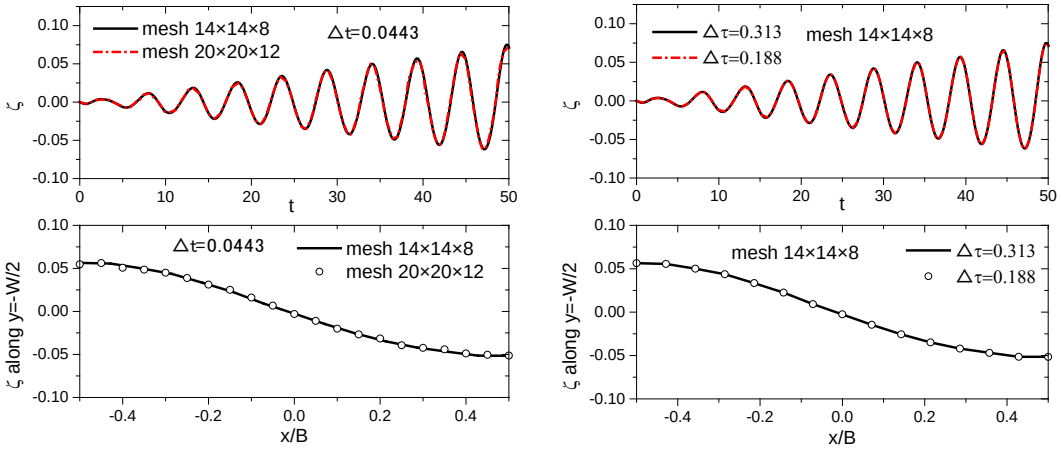

(a) Mesh size convergence analysis (b) Time step convergence analysis

Fig. 7. Results of convergence analysis

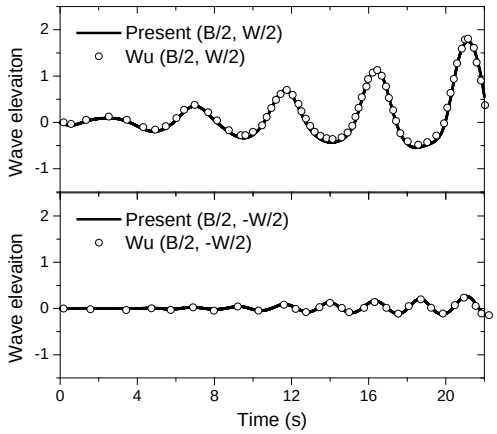

Fig. 8. 3D sloshing wave elevation histories

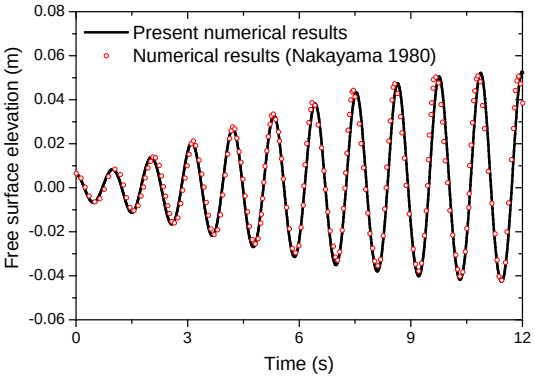

Fig. 9. Wave elevation histories due to rotational excitation

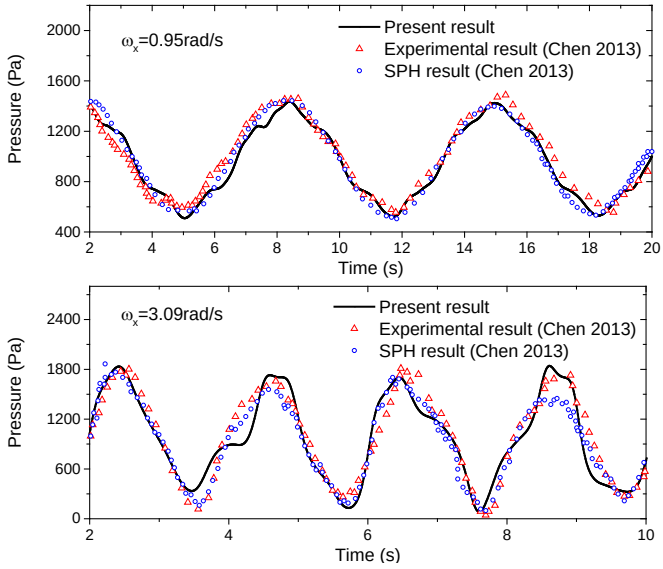

Fig. 10. Pressure histories due to rotational excitation

In addition, vessel motion solutions based on impulsive response function and the coupling calculation of liquid loading vessel motions are validated by experimental tests conducted by Rognebakke and Faltinsen (2003). The test results of solid and liquid loading conditions serve as the validation of vessel motion calculation and coupling calculation, respectively. In Rognebakke's experiments, a rectangular hull containing two liquid tanks is restricted to sway motion in waves, as shown in Fig. 11. Responses of the solid loading condition and liquid loading condition with two tanks of 0.186 *m* filling level are selected for comparison with numerical results. Element numbers along the length, width and water depth of each liquid tank are set as $8\times18\times10$. Fig. 12 shows the comparison of sway response amplitude operators (RAOs). The proposed numerical model can give good prediction of vessel motions as well as coupling interaction with internal sloshing.

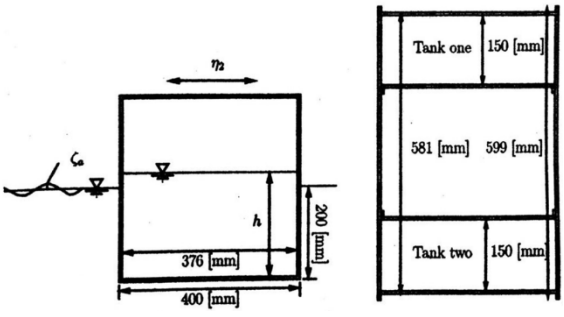

Fig. 11 Liquid loading hull sections

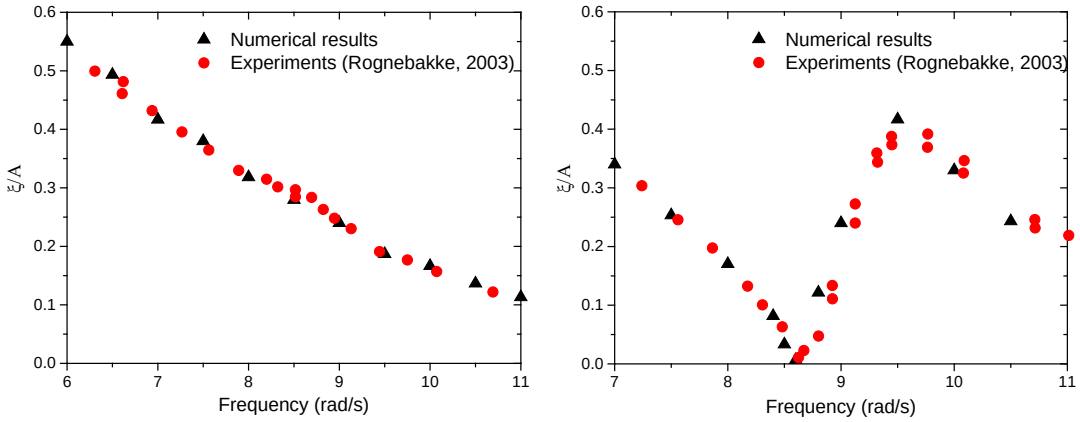

Fig. 12. RAOs of sway in solid and liquid loading conditions

6. Results and discussion

Coupling interactions between vessel motion and internal sloshing are investigated using the newly developed numerical code and experimental tests. The coupling mechanism is first analyzed based on coupling responses in beam sea conditions. Then, considering an FLNG vessel subjected to varying filling levels and wave directions corresponding to the offloading operation and weather-vaning characteristics of a single-point mooring system, the sensitivities of coupling effects to filling level and wave direction are studied.

6.1 Coupling interaction of liquid loading vessel

In this section, the coupling mechanism is investigated based on the responses of vessel motions and sloshing under beam sea conditions. A 66.7% filling level is considered, and the wave amplitude is set as 0.9 *m*. According to existing experimental results (Zhao et al., 2015), the artificial damping coefficient described in (13) is selected as $\mu = 0.1$ in the numerical model of sloshing calculation. Experimental results of solid and liquid loading conditions in beam white noise waves are adopted for comparison. The natural sloshing frequencies of the three-dimensional rectangular tank can be expressed analytically as follows (Faltinsen and Timokha, 2009):

$$\omega_{mn} = \sqrt{\pi\sqrt{(\frac{m^2}{B^2}+\frac{n^2}{W^2})}\tanh(\pi\sqrt{(\frac{m^2}{B^2}+\frac{n^2}{W^2})})} \tag{30}$$

where m and n are positive integers, the tank size are non-dimensionalized based on water depth D

Decay tests in still water can easily capture the sloshing effects on vessel motion. Decay tests results of solid and liquid loading conditions are listed in Table 2. It can be seen that liquid loading conditions tend to have larger periods and damping coefficients in roll and pitch modes. Small differences are observed in heave decay motion between the two loading conditions.

Motion responses of solid and liquid loading vessels are transformed into the frequency domain. RAOs of a vessel's responses under white noise waves can be calculated as follows:

$$H(\omega) = \sqrt{S_y(\omega)/S_x(\omega)} \tag{31}$$

where $S_x(\omega)$ and $S_y(\omega)$ are power spectrum densities of white noise wave and the responses of the vessel, respectively. The transfer function of sloshing is also defined as the ratio between sloshing amplitude and wave amplitude. Comparisons of RAO results in Fig. 13 show that numerical results agree well with experimental results in both solid and liquid loading conditions. Comparing motion responses in solid and liquid loading conditions reveals that the sway and roll motions of the vessel are significantly affected by sloshing. To be specific, in the liquid loading condition, very small sway and roll motion responses are induced near the first sloshing natural frequency (0.886 *rad/s*). When wave frequencies are larger than 0.886 *rad/s*, responses begin to increase and a small peak can be found from sway motion in the liquid loading condition. A much smaller peak can also be observed from the roll motion mode. In addition, heave motion is less affected by liquid sloshing in tanks and highly similar heave motion responses are induced in these two loading conditions. The reason is that the sloshing force in the vertical direction varies slightly when sloshing occurs (Ibrahim, 2005; Zhao et al., 2015). Moreover, the natural frequency of roll motion decreases from approximately 0.48 *rad/s* in the solid loading condition to 0.42 *rad/s* in the liquid loading condition, which coincides with the decay test results in Table 2. This tendency indicates that liquid in tanks leads to a loss of restoring force and induces a longer natural roll period. The peak amplitude of roll motion response in natural frequency is also decreased, which corresponds to the increased damping coefficient presented in Table 2. In terms of sloshing responses, Fig. 14 shows the spectra of wave elevation in location T1 and numerically calculated sloshing loads in sway and roll modes. Two obvious peaks appear in the natural roll frequency and in the frequency region that is higher than natural sloshing frequency. Specifically, much larger sloshing loads in the sway mode appear in the second peak than in the first peak, while sloshing loads in the roll mode and sloshing wave elevation have larger responses in the first peak. This pattern indicates that sloshing loads in different modes are not linearly related with sloshing wave elevation.

Table 2 Decay results of vessel in solid and in liquid loading conditions

		Solid loading	Liquid loading
Heave	Period (s)	10.17	10.41
	Damping coefficient	0.2163	0.2216
Roll	Period (s)	13.04	14.93
	Damping coefficient	0.0082	0.0096
Pitch	Period (s)	9.68	9.53
	Damping coefficient	0.1284	0.1392

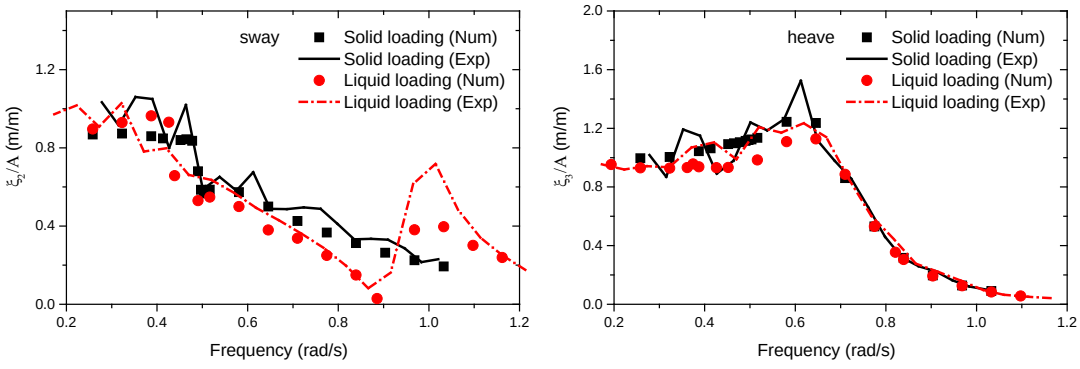

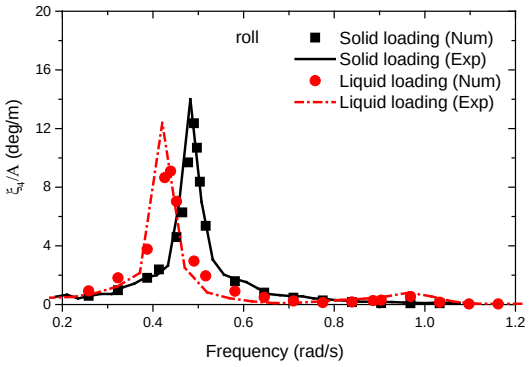

Fig. 13 RAOs of vessel motions under beam sea

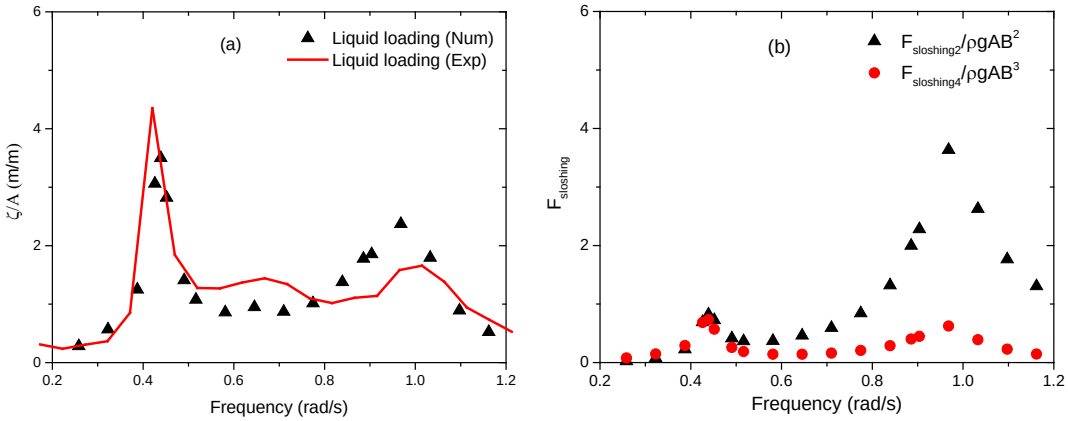

Fig. 14 Sloshing responses under beam sea; (a) Transfer function of sloshing amplitude in T1, (b) sloshing loads

The influences of a vessel's sway and roll motions on sloshing vary in different frequencies. Roll and sway motions are the main excitation forces on sloshing near the natural roll motion and natural sloshing frequency region, respectively. Fig. 15 gives the phase shifts of sway and roll motions to wave elevation in T1 (defined as $\sigma_{ship\ motion} - \sigma_{sloshing\ elevation}$, where σ stands for phase). This figure indicates that wave elevation has a small phase shift with roll motion in the low-frequency region and has a small phase shift with sway motion in the high-frequency region. In detail, the histories of sway, roll motions and wave elevation in representative frequencies (0.426, 0.481, 0.878, 0.968 *rad/s*) are plotted in Fig. 16. The histories of sloshing loads and corresponding wave loads in these cases are plotted in Fig. 17. In the natural roll frequency of liquid loading condition ($\omega = 0.426 rad/s$), wave elevation has the same phase as roll motion and has a phase shift approximately 90 degrees with sway motion, which indicates that sloshing waves are mainly induced by roll motion. The reason is that 0.426 *rad/s* is a relatively low frequency compared with the first natural sloshing frequency. The inclination of a liquid tank related to the ship's roll motion rather than sway excitation is the main factor producing of sloshing. Fig. 17 shows that sloshing momentums contribute positively to the roll motion in that case. As a result, large roll motion is induced, as indicated in Fig. 13. When the excitation frequency increases to the natural roll frequency of the liquid loading condition (0.481 *rad/s*), sway motion has almost the opposite excitation on liquid sloshing with roll motion; the small phase shift between roll motion and sloshing wave elevation indicates that roll motion is still the dominant excitation of sloshing. However, sloshing force has an opposite phase with wave force in roll mode, which

leads to a smaller roll motion response than in the solid loading condition. When the wave frequency is close to the first natural sloshing frequency (0.878 *rad/s*), as shown in Fig. 15, the sloshing phase is opposite the sway and roll motions. As liquid sloshing is in a resonant condition, even small sway and roll motions can excite significant sloshing responses, as shown in Fig. 14. Fig. 17 shows that sloshing loads have similar amplitude but opposite phase as wave loads, which leads to slightly excited ship sway and roll motions. In the case 0.968 *rad/s*, for the solid loading condition, this excitation frequency is away from the main response frequency region of the ship, and very small responses are excited by waves, as shown in Fig. 13. For liquid loading conditions, 0.968 *rad/s* is close to the natural sloshing frequency and sloshing responses can also be very dramatic. As shown in Fig. 15, sloshing loads are much larger than corresponding wave loads and play a dominant role in the excitation of vessel motions. Consequently, obvious sway response peaks can be observed in this frequency region in Fig. 13. The phase properties shown in Figs. 15-17 also show that sway motion is the main excitation of induced sloshing.

Sloshing wave profiles corresponding to the largest wave elevations in the cases 0.426 *rad/s* and 0.968 *rad/s* are plotted in Fig. 18. The tank inclination that caused sloshing in the case 0.426 *rad/s* has a flat free surface, while the sway motion-induced wave profile in case 0.968 *rad/s* is much more curved and exhibits a first mode property. Fig. 19 shows the snapshots of the free surface in the case $\omega = 0.426 rad/s$ in the experiment. As the video camera is fixed in the ship model, roll motion cannot be observed directly. The basin bank is marked by a dashed line in Fig. 19 as a reference. Clearly, the sloshing free surface in the tank is rather flat and almost parallel with the basin bank. The sloshing elevation is in the same phase as roll motion (the angle between basin bank and the upper deck of the vessel model). As noted above, the reason is that roll motion is the main excitation of sloshing. The surface profile and phase properties coincide well with the numerical results in Figs. 16 and 18 (b).

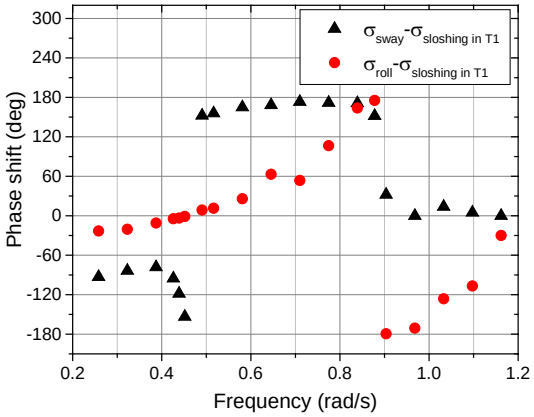

Fig. 15 Phase shifts of sway and roll motions to sloshing wave elevation in T1

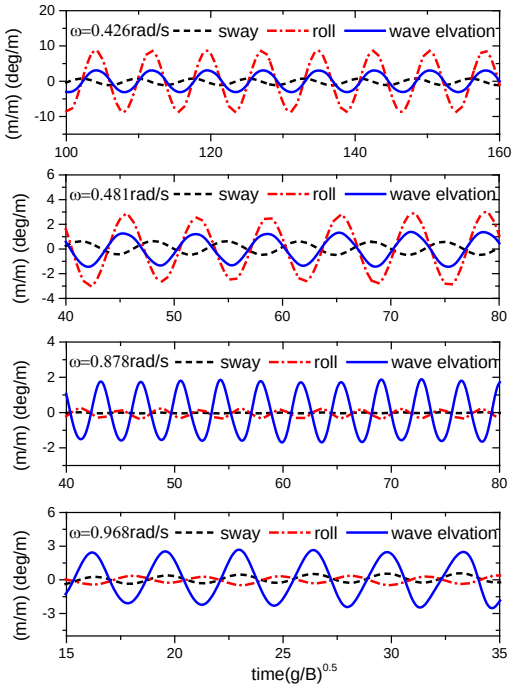

Fig. 16 Sway and roll motions and sloshing wave elevation histories under different frequencies

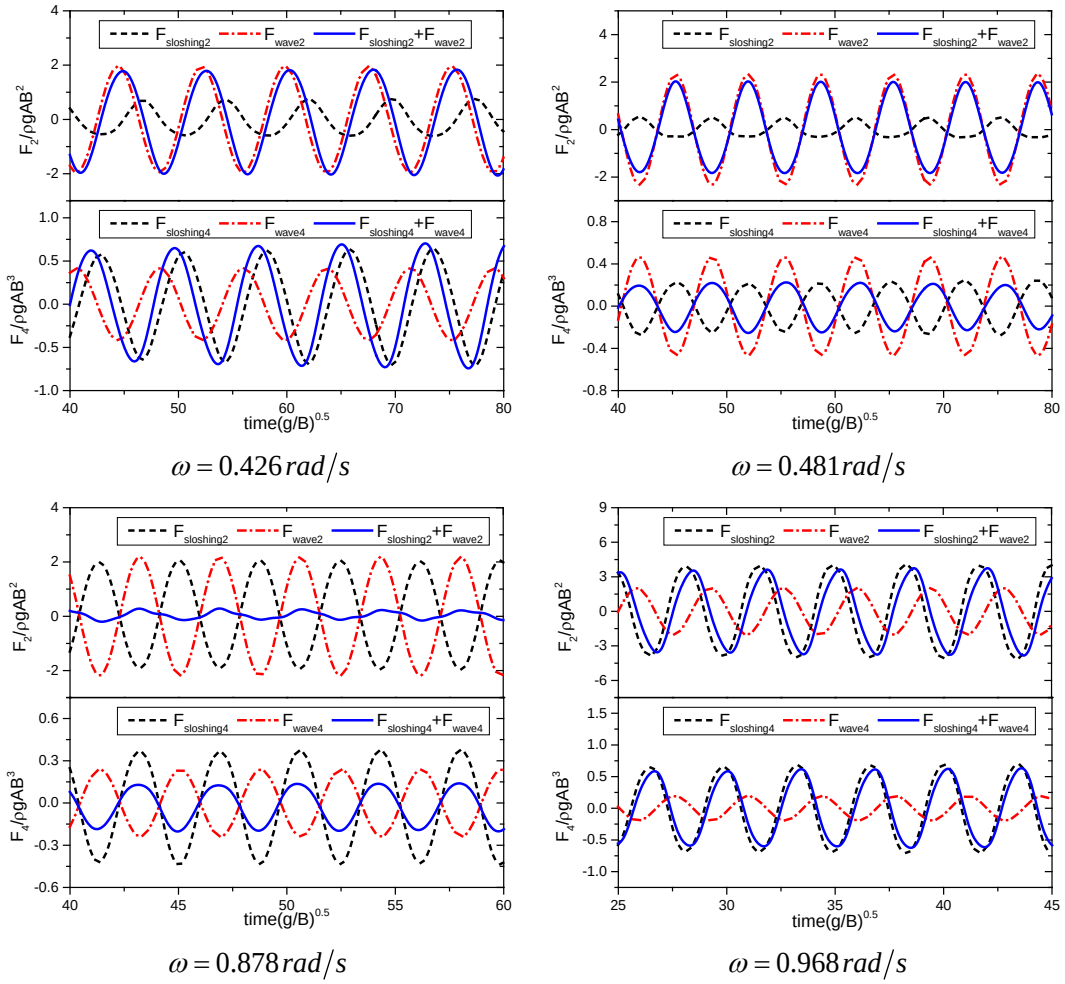

Fig. 17 Wave and sloshing load histories under different wave frequencies

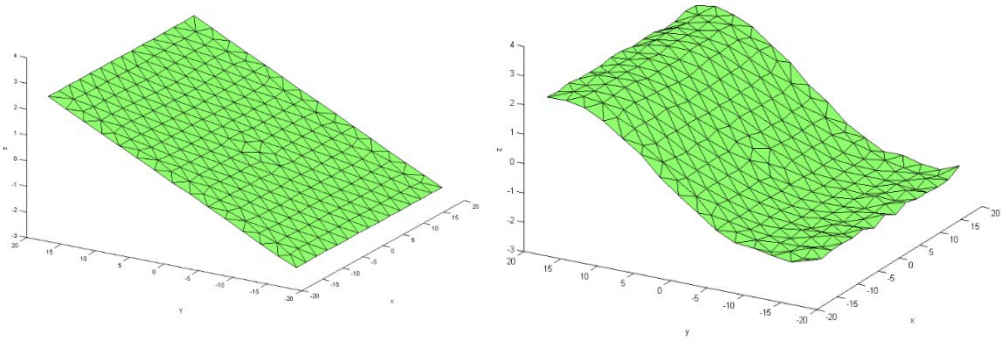

(a) $\omega = 0.426\,rad/s$ (b) $\omega = 0.968\,rad/s$

Fig. 18 Sloshing wave profiles under different frequencies

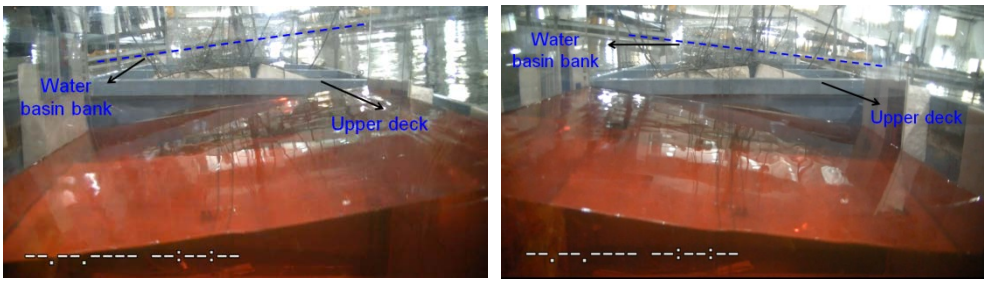

Fig. 19 Snapshots of sloshing free surface in tank 1 under wave frequency $\omega = 0.426\,rad/s$

6.2 Sensitivity studies

The sensitivities of coupling responses to filling level and wave amplitude are discussed in this section. Five liquid loading cases are selected, as shown in Table 3. Three filling levels are selected with liquid tanks 22.2%, 44.4% and 66.7% filled. Beam wave is considered in the calculation. To avoid the situation where sloshing wave elevation becomes larger than water depth in the liquid tank, a small wave amplitude, A=0.09 m, is selected in the 22.2% filling condition. Wave amplitudes are doubled in Cases D and E to investigate sloshing nonlinearity effects. Wave amplitudes and first mode sloshing natural frequencies calculated based on (30) are presented in Table 3.

Table 3 Wave and sloshing parameters in different filling levels in prototype scale

Case	A	B	C	D	E
Filling level	22.2%	44.4%	66.7%	22.2%	66.7%
Wave amplitude (m)	0.09	0.9	0.9	0.18	1.8
ω_{01} (rad/s)	0.641	0.818	0.886	0.641	0.886

Vessel motion and sloshing responses in Cases A to C are analyzed to investigate filling level effects. The results in the frequency domain are plotted in Fig. 20. It can be determined that heave motions in the three filling levels have little difference and are similar to the heave motion response in the solid loading condition, which indicates that heave motion is less affected by sloshing in liquid tanks. For Cases B and C, sway motions are smaller than those in the solid loading condition, except in the high frequency, where larger sway motions are induced for liquid

sloshing. In the corresponding sloshing natural frequencies, the sway motion amplitudes in these two loading conditions are close to zero. Cases B and C also have lower peak roll motion than the solid loading condition. However, the roll motion natural frequency in Case B is not decreased due to sloshing effects as in Case C. The non-dimensionalized sloshing responses in Fig. 20 show that although similar wave elevation amplitudes are excited in Cases B and C, sloshing loads on the ship are much smaller in Case B for small liquid mass. The large sloshing momentum in Case C is formed not only by the hydrodynamic sloshing load but also by static loads related to roll motion, which is much larger than the other two filling conditions for its high filling level. For Case A with a 22.2% filling level, the sloshing natural frequency is smaller and close to the main response frequency region of a ship's sway and roll motions. Thus, much different coupling effects are induced. It can be observed that two consecutive peaks corresponding to natural roll motion and sloshing frequencies are formed in both roll motion and sloshing responses. Though sway motion is still decreased near the natural sloshing frequency, it is no closer to zero in the natural sloshing frequency. Sway and roll motions all have much larger amplitudes in the second peak region caused by internal sloshing. Under the increased vessel motion excitations, Case A also has significant sloshing wave elevations as well as sloshing force in the sway direction. However, compared with Case C, this enhanced sloshing contributes less to sloshing momentum on ships for the small liquid mass. Natural roll motion frequency has a slight increase towards the natural sloshing frequency, which is different from Cases B and C.

Phase shifts of sloshing forces to wave forces in Cases A, B and C are calculated to investigate sloshing contribution to loads on the vessel. Fig. 21 clearly shows that 44.4% and 66.7% filling conditions have similar phase shift properties. In these two filling conditions, the phase shifts of sloshing forces to wave forces in sway and roll modes are similar, which is also proven by force histories in Fig. 15. Phase shifts increase rapidly near the natural roll motion frequencies and exhibit a sudden change in natural sloshing frequencies. A small phase shift exists in the low-frequency region smaller than the roll motion natural frequency and the high-frequency region larger than the natural sloshing frequency. Therefore, for Cases B and C, larger motion responses are excited in these two frequency regions, as shown in Fig. 20. Between the natural roll motion and sloshing frequencies, phase shifts are close to 180 degrees, which corresponds to smaller motion responses in Fig. 20. For Case A, phase shifts of sloshing force to wave force in the sway mode have a tendency similar to that of phase shifts in the other two filling conditions. Except in the small region between roll motion and natural sloshing frequencies (0.5 rad/s—0.7 rad/s), the sloshing force in the sway mode has positive influences on wave force in a wide frequency region and leads to large sway motion responses in this frequency region (Fig. 20). However, in Case A, roll mode has the opposite phase shift distribution as sway mode. Only between the natural roll motion and sloshing frequencies does the sloshing force in the roll mode contribute positively to larger roll motion responses (Fig. 20).

Effects of nonlinear free surface can be observed from a comparison of results in Cases A and C with those in Cases D and E, as shown in Fig. 22. Fig. 22 (a) to (d) show that, with the exception of a slight decrease of sway motion in Case E, sway and roll motions are linear with wave amplitudes. The histories of sloshing waves in Fig. 22 (e) and (f) show increased sloshing nonlinearity under large wave amplitude, especially in the 22.2% fill condition. However, the sloshing nonlinearity contributes less to the motions of the vessel.

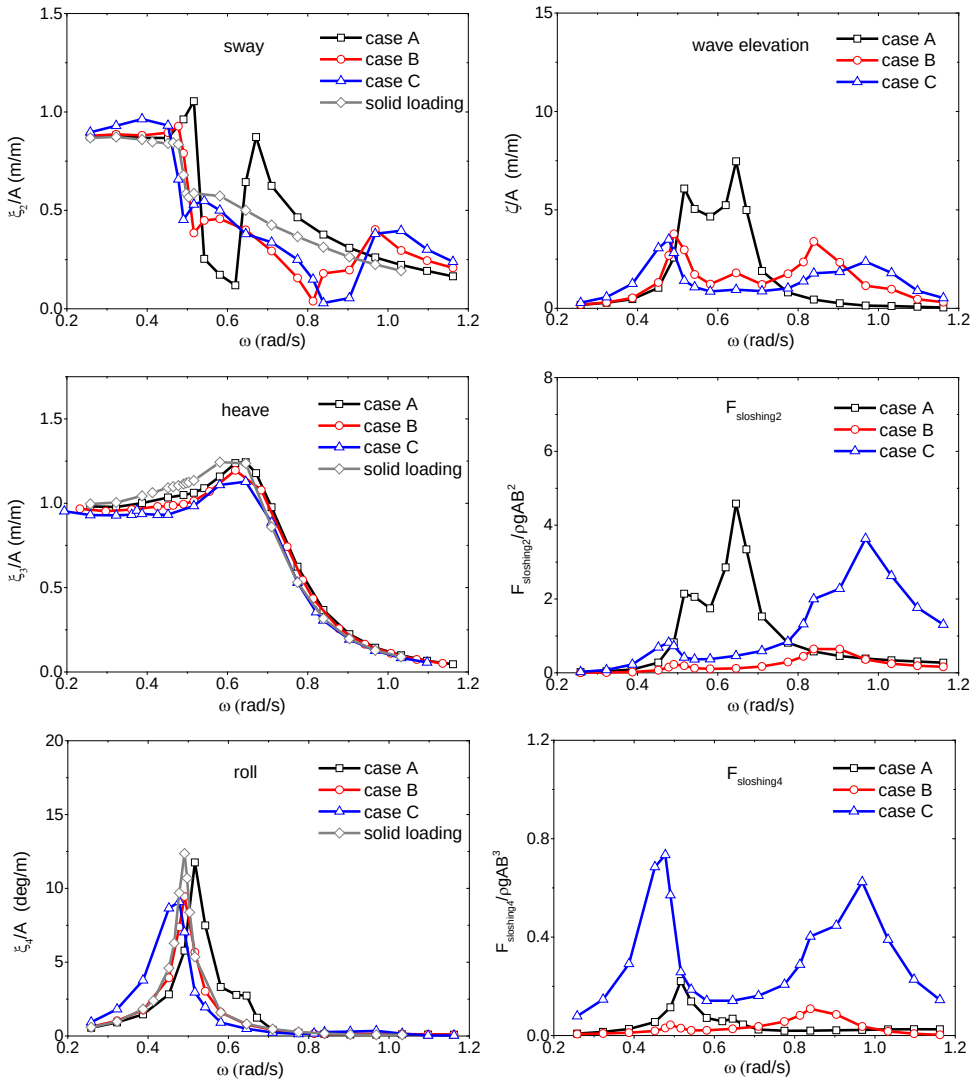

Fig. 20 Motion RAOs and sloshing responses of three filling conditions under a beam sea

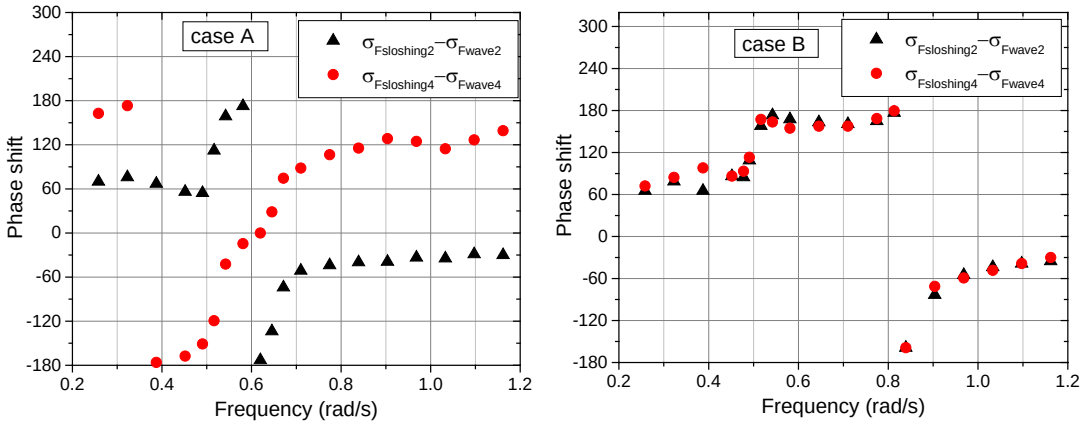

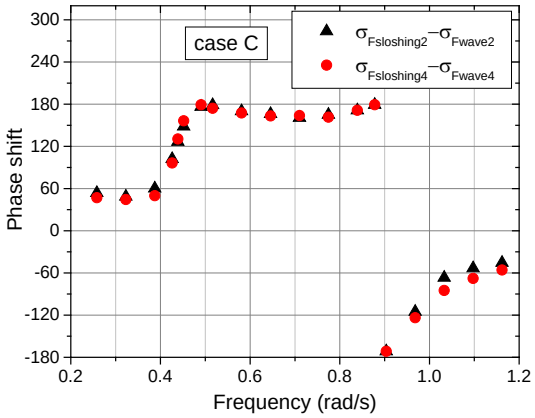

Fig. 21 Phase shifts of sloshing loads to wave loads

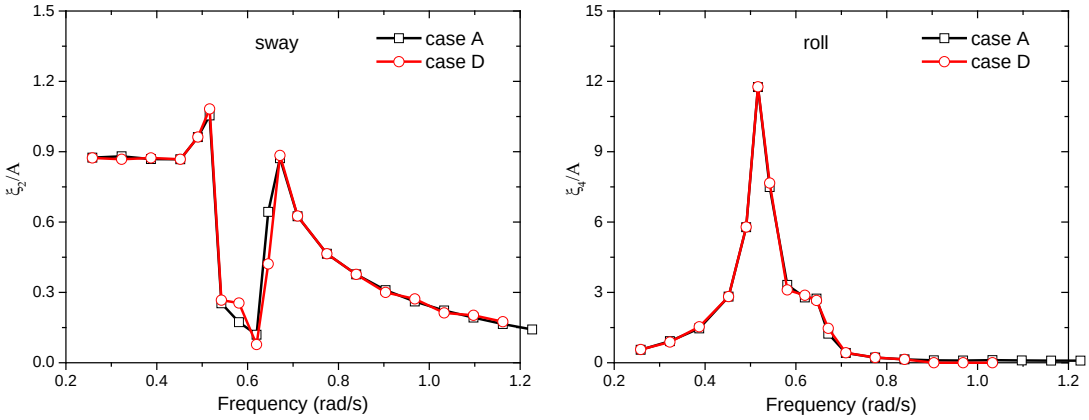

(a)

(b)

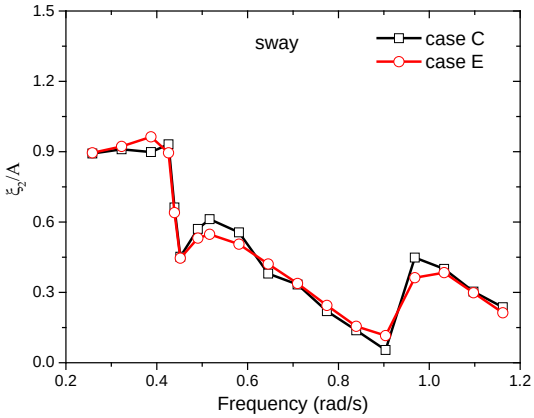

(c)

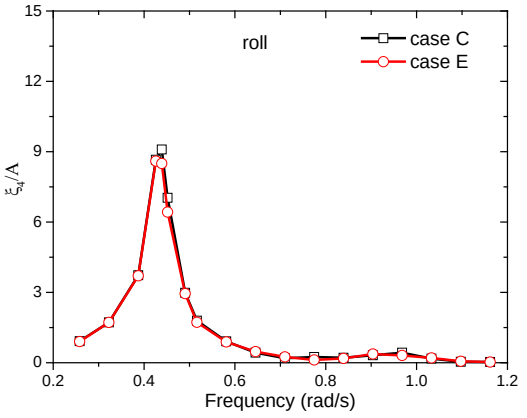

(d)

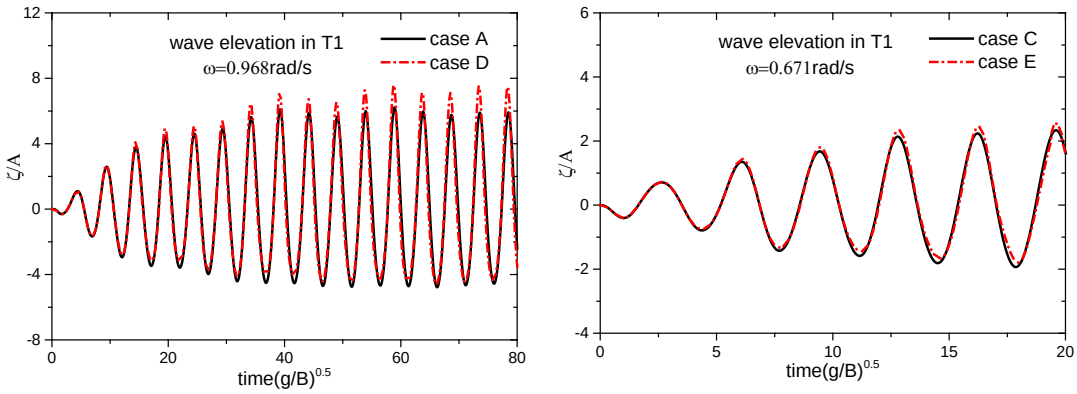

(e) (f)

Fig. 22 Influences of wave amplitude to motion responses and wave sloshing

6.3 Wave direction effects

For an FLNG system with a single-point mooring system, FLNG vessel motion demonstrates weather-vaning characteristics. Coupling properties under different wave directions are investigated in this section. Solid and liquid loading conditions at 66.7% filling level are selected, and responses under head and quarter waves are analyzed.

In the head wave condition, surge and pitch motions play similar roles in coupling with liquid sloshing as sway and roll motions under a beam sea condition. However, for the differences in restoring coefficients and wave forces, different coupling results are induced. Vessel motion RAOs in solid and liquid loading conditions are shown in Fig. 23, and good agreements between numerical and experimental results are obtained. Generally, in head waves, the liquid sloshing has no significant effects on vessel motions as in a beam sea. Sloshing elevation RAOs in Fig. 24 reveal that both surge and pitch motions contribute less to liquid sloshing in their main response frequency regions (0.2-0.6 *rad/s*); no wave elevation peak can be found within that region as in the beam sea condition. Nevertheless, in the liquid loading condition, the coupled surge motion under the head wave shows similarities to the sway motion in a beam sea. The surge motion response is also close to zero in the natural sloshing frequency. A small response peak appears in the higher frequency region for sloshing coupling effects, which corresponds to the peak in sloshing wave elevation in Fig. 24. In addition, pitch motion excitation on the two liquid tanks tends to have different directions for the two tanks located on the two sides of the midship, which will mitigate sloshing effects on pitch motion. Thus, sloshing effects on pitch motion responses are limited.

In quartering waves, the ship's 6 DOF motions are all coupled with liquid sloshing. Coupling properties derived in beam and head sea conditions can all be observed in quarter sea conditions. Moreover, yaw motion exhibits coupling phenomena under quartering waves. As shown in Fig. 25, sloshing effects on yaw are much more similar to those on surge motion, which has a small response peak in the high-frequency region. The reason may be that yaw motion frequency is generally larger than liquid sloshing and coupling effects are not very obvious. The wave elevation RAO in Fig. 26 shows that two response peaks are excited in beam sea conditions. Wave elevation histories in the four corners of Tank 1 are plotted in Fig. 27. In the low-frequency $\omega = 0.452\,rad/s$, the wave elevations in the four corners have the same amplitudes, T1 and T4 located in the starboard side have the opposite phases with T2 and T4 located in the portside. This

indicates that roll motion rather than pitch motion is the main excitation on liquid sloshing. In the high frequency $\omega = 0.968 rad/s$, wave elevations on the diagonal have the same amplitude but opposite phase. Sloshing in T1 and T3 have larger amplitude than in T2 and T4. The reason is that both surge and sway motions contribute to sloshing in the liquid tank. The phase shift between surge and sway motions causes the different sloshing amplitudes between corners.

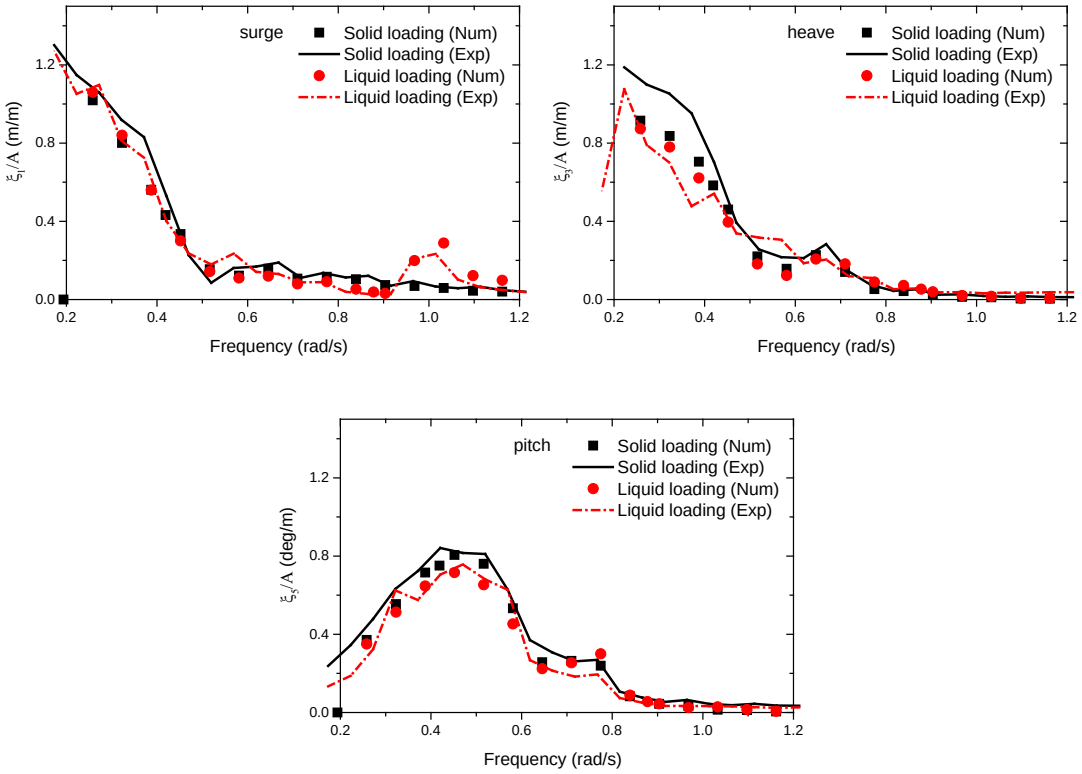

Fig. 23 RAOs of solid and liquid loading conditions under head sea

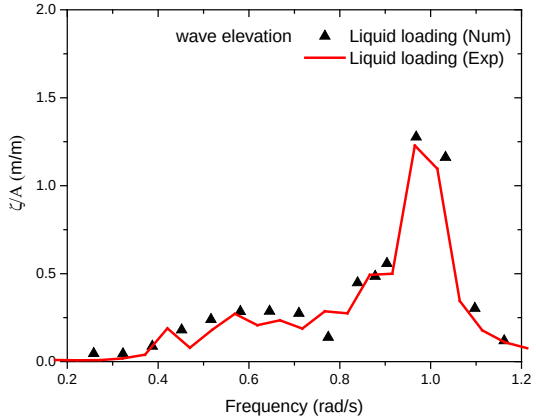

Fig. 24 Transfer function of sloshing amplitude in T1 under head sea

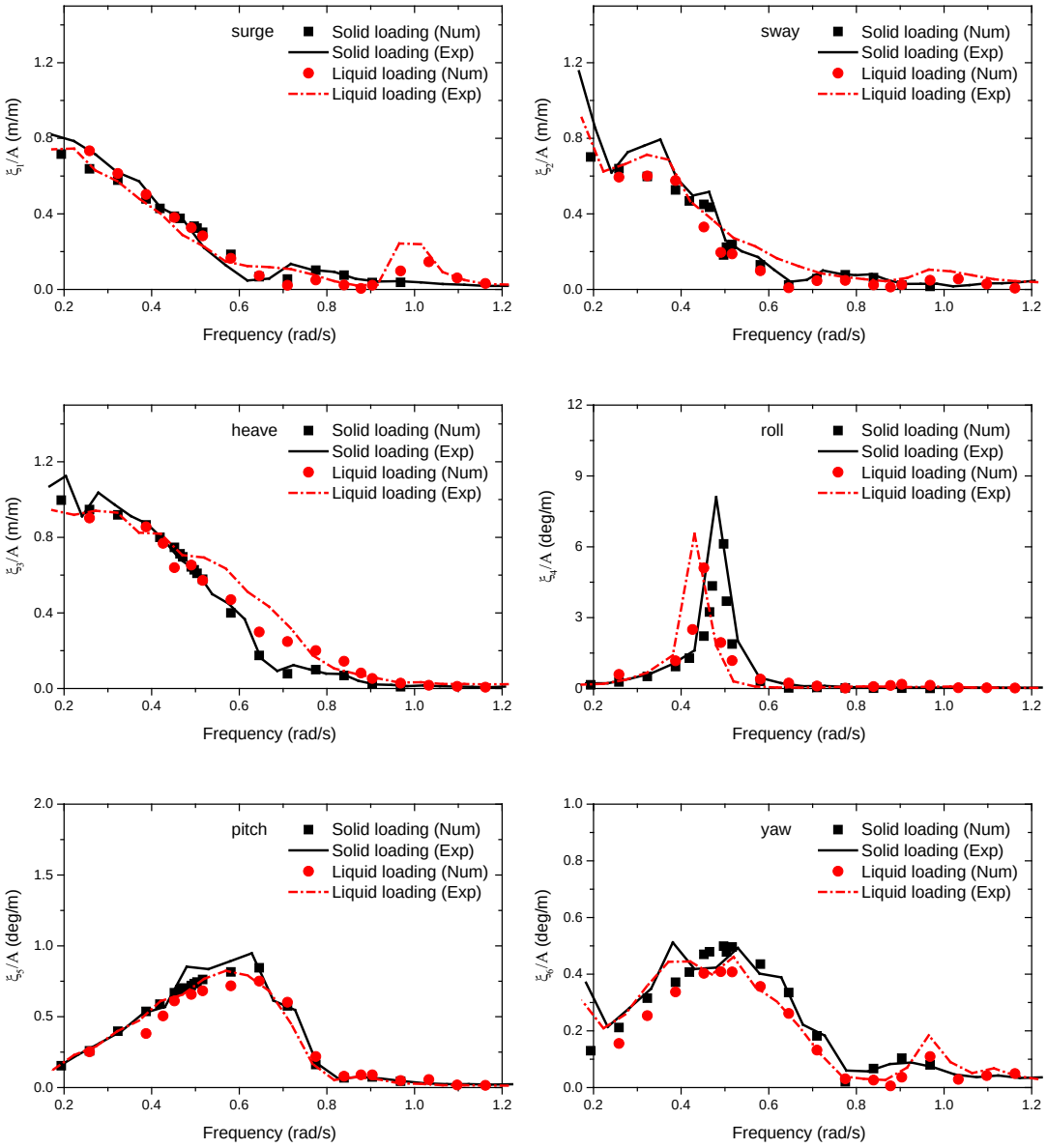

Fig. 25 RAOs of solid and liquid loading conditions under quarter sea

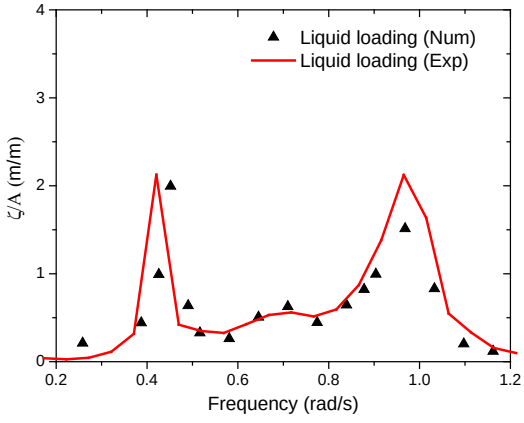

Fig. 26 Transfer function of sloshing amplitude in T1

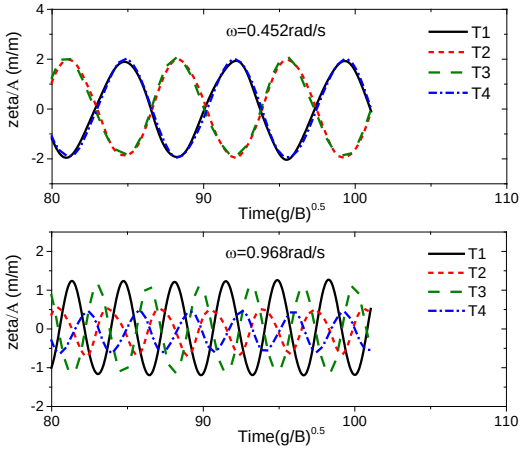

Fig. 27 Sloshing wave elevation histories in tank 1

7. Conclusion

An efficient numerical model is developed in this study to analyze the coupling interaction between FLNG vessel motions and liquid sloshing in tanks. Experimental tests are conducted to validate the numerical code and provide a better perceptual understanding of the coupling mechanism. Based on systematic calculations and discussions, the sloshing effects on vessel motions are studied. Coupling properties in different filling levels and sea conditions are demonstrated. The following conclusions are drawn:

1) Significant coupling effects can be induced in beam sea conditions between sway and roll motions and internal sloshing; heave motion is slightly affected by internal sloshing.
2) Sloshing responses are mainly excited in the natural roll motion and natural sloshing frequencies. Coupling effects will increase rapidly when the natural sloshing frequency is close to the main response frequency region of the ship.
3) When the natural sloshing frequency is larger than the main response frequency region of the vessel, sloshing responses in liquid tanks in low- and high-frequency regions are mainly affected by roll motion and sway motion, respectively. The phase shift between wave loads and sloshing loads shows rapid change near the natural roll motion and natural sloshing frequencies.
4) The sloshing nonlinearity increases obviously under large wave amplitude, and RAOs of a liquid loading vessel’s motions are nearly independent of wave amplitudes.
5) Coupling effects under a head sea have similar properties to these in a beam sea, but surge and pitch motions are less sensitive to sloshing than sway and roll motions in a beam sea.

Acknowledgements

This work was supported by State Key Lab of Ocean Engineering Shanghai Jiao Tong University and the State Key Lab of Hydraulic Engineering Simulation and Safety Tianjin University and financially supported by China National Scientific and Technology Major Project (Grant No. 2016ZX05028-006-009), (Grant No. HESS-1404); and all of these supports are gratefully acknowledged by the authors.

References

Cercos-Pita, J. L., Bulian, G., Pérez-Rojas, L., & Francescutto, A. (2016). Coupled simulation of nonlinear ship motions and a free surface tank. *Ocean Engineering*, *120*, 281-288.

Chen, Y. H., Hwang, W. S., & Ko, C. H. (2007). Sloshing behaviors of rectangular and cylindrical liquid tanks subjected to harmonic and seismic excitations. Earthquake Engineering & Structural Dynamics, 36(12), 1701-1717.

Chen, Z., Zong, Z., Li, H. T., & Li, J. (2013). An investigation into the pressure on solid walls in 2D sloshing using SPH method. *Ocean Engineering*, *59*, 129-141.

Cummins, W. E. (1962). *The impulse response function and ship motions* (No. DTMB-1661). David Taylor Model Basin Washington DC.

Faltinsen, O. M. (1974). A nonlinear theory of sloshing in rectangular tanks. *Journal of Ship Research*, *18*(4).

Faltinsen, O. M.(1993). Sea loads on ships and offshore structures (Vol. 1). Cambridge university press.

Faltinsen, O. M., & Timokha, A. N. (2001). An adaptive multimodal approach to nonlinear sloshing in a rectangular tank. *Journal of Fluid Mechanics*, *432*, 167-200.

Faltinsen, O. M., & Timokha, A. N. (2009). Sloshing.

Grilli, S. T., & Svendsen, I. A. (1990). Corner problems and global accuracy in the boundary element solution of nonlinear wave flows. *Engineering Analysis with Boundary Elements*, *7*(4), 178-195.

Hu, Z. Q., Wang, S. Y., Chen, G., Chai, S. H., & Jin, Y. T. (2016). The effects of LNG-tank sloshing on the global motions of FLNG system. *International Journal of Naval Architecture and Ocean Engineering*.

Huang, S., Duan, W., & Zhang, H. (2012). A coupled analysis of nonlinear sloshing and ship motion. *Journal of Marine Science and Application*, *11*(4), 427-436.

Hunter, P., & Pullan, A. (2001). Fem/bem notes. *Department of Engineering Science, The University of Auckland, New Zeland*.

Ibrahim, R. A. (2005). *Liquid sloshing dynamics: theory and applications*. Cambridge University Press.

Jiang, S. C., Teng, B., Bai, W., & Gou, Y. (2015). Numerical simulation of coupling effect between ship motion and liquid sloshing under wave action. *Ocean Engineering*, *108*, 140-154.

Kim, Y. (2001). Numerical simulation of sloshing flows with impact load. *Applied Ocean Research*, *23*(1), 53-62.

Kim, Y., Nam, B. W., Kim, D. W., & Kim, Y. S. (2007). Study on coupling effects of ship motion and sloshing. *Ocean Engineering*, *34*(16), 2176-2187.

Lee, S. J., Kim, M. H., Lee, D. H., Kim, J. W., & Kim, Y. H. (2007). The effects of LNG-tank sloshing on the global motions of LNG carriers. *Ocean Engineering*, *34*(1), 10-20.

LI, Y. L., ZHU, R. C., MIAO, G. P., & Ju, F. A. N. (2012). Simulation of tank sloshing based on OpenFOAM and coupling with ship motions in time domain. *Journal of Hydrodynamics, Ser. B*, *24*(3), 450-457.

Malenica, S., Zalar, M., & Chen, X. B. (2003). Dynamic coupling of seakeeping and sloshing. In *13th International Offshore and Polar Engineering Conference, ISOPE, Honolulu, HI, May* (pp. 25-30).

Mitra, S., Wang, C. Z., Reddy, J. N., & Khoo, B. C. (2012). A 3D fully coupled analysis of nonlinear sloshing and ship motion. *Ocean Engineering*, *39*, 1-13.

Nakayama, T., & Washizu, K. (1981). The boundary element method applied to the analysis of two-dimensional nonlinear sloshing problems. International Journal for Numerical Methods in Engineering, 17(11), 1631-1646.

Nam, B. W., Kim, Y., Kim, D. W., & Kim, Y. S. (2009). Experimental and numerical studies on ship motion responses coupled with sloshing in waves. *Journal of Ship Research*, *53*(2), 68-82.

Nasar, T., Sannasiraj, S. A., & Sundar, V. (2010). Motion responses of barge carrying liquid tank. *Ocean Engineering*, *37*(10), 935-946.

Newman, J. N. (2005). Wave effects on vessels with internal tanks. In *Proceedings of the 20th Workshop on Water Waves and Floating Bodies, Spitsbergen, Norway*.

Ning, D. Z., Teng, B., Zhao, H. T., & Hao, C. L. (2010). A comparison of two methods for calculating solid angle coefficients in a BIEM numerical wave tank. *Engineering analysis with boundary elements*, *34*(1), 92-96.

Ogilvie, T. F. (1964, September). Recent progress toward the understanding and prediction of ship motions. In *5th Symposium on naval hydrodynamics*(Vol. 1, No. 2, pp. 2-5). Bergen, Norway.

Rognebakke, O. F., & Faltinsen, O. M. (2003). Coupling of sloshing and ship motions. *Journal of Ship Research*, *47*(3), 208-221.

Serván-Camas, B., Cercós-Pita, J. L., Colom-Cobb, J., García-Espinosa, J., & Souto-Iglesias, A. (2016). Time domain simulation of coupled sloshing–seakeeping problems by SPH–FEM coupling. *Ocean Engineering*, *123*, 383-396.

Tanizawa, K. (1995). A nonlinear simulation method of 3-D body motions in waves formulation with the acceleration potential. In *10h Workshop on Water Waves and Floating Bodies, Oxford*.

Teng, B., Gou, Y., & Ning, D. Z. (2006). A higher order BEM for wave-current action on structures-Direct computation of free-term coefficient and CPV integrals. *China Ocean Engineering*, *20*(3), 395-410.

Wu, G. X., Ma, Q. W., & Taylor, R. E. (1998). Numerical simulation of sloshing waves in a 3D tank based on a finite element method. *Applied Ocean Research*, *20*(6), 337-355.

Zhang, C. (2016). Nonlinear simulation of resonant sloshing in wedged tanks using boundary element method. *Engineering Analysis with Boundary Elements*, *69*, 1-20.

Zhao, D., Hu, Z., & Chen, G. (2015). An investigation on two dimensional nonlinear sloshing in rectangular tank. In *ASME 2015 34th International Conference on Ocean, Offshore and Arctic Engineering* (pp. V001T01A045-V001T01A045). American Society of Mechanical Engineers.

Zhao, W. (2013). Hydrodynamics and design analysis of an FLNG system. *Ph.D. Thesis, Shanghai Jiaotong University, China*.

Zhao, W., & HU ZQ, Y. J. (2011). Investigation on sloshing effects of tank liquid on the FLNG vessel responses in frequency domain [J]. *Journal of ship mechanics*, *3*, 227-237.

Zhao, W., Yang, J., Hu, Z., & Tao, L. (2014). Coupled analysis of nonlinear sloshing and ship motions. *Applied Ocean Research*, *47*, 85-97.